

# Free Vibration Analysis of a Simplified Compressor Blade Modeled as a Rectangular Plate with NACA 2412 Thickness Distribution

Saroj Basnet

Graduate Student, Department of Mechanical Engineering, Pulchowk Campus, Institute of Engineering, Tribhuvan University, Nepal

---

## Abstract

Compressor blades in modern engines experience complex mechanical and aerodynamic forces, making vibration analysis essential for safety and performance. This study investigates the free vibration of a simplified compressor blade modeled as a rectangular plate with a NACA 2412 variable thickness distribution. The model is developed using Reissner–Mindlin plate theory and the Rayleigh–Ritz method, assuming a clamped–free–free–free boundary condition. Stiffness and mass matrices are evaluated using Gaussian quadrature, and the resulting eigenvalue problem yields the natural frequencies and mode shapes. The predicted frequencies show excellent agreement with ANSYS finite element results, with differences below 3% for the first six modes and under 7% for higher modes. Modal energy analysis indicates that lower modes are dominated by bending deformation, while higher modes exhibit increasing shear and in-plane membrane effects. The results demonstrate that this reduced-order, semi-analytical model can accurately capture the key vibration characteristics of compressor blades with far lower computational cost than full finite element models.

**Keywords:** NACA 2412 airfoil; Reissner-Mindlin plate theory; Rayleigh-Ritz method; Free vibration analysis; Mode shapes

## Nomenclature

### Geometric and Material Properties

**a:** Length of the blade in the spanwise (x) direction (m)

**b:** Width (chord length) of the blade in the chordwise (y) direction (m)

**E:** Young's modulus of the blade material (Pa)

**v:** Poisson's ratio of the blade material

**$\rho$ :** Density of the blade material ( $\text{kg}/\text{m}^3$ )

**G:** Shear modulus of the blade material (Pa)

**$h(y)$ :** Thickness distribution function along the chord, derived from the NACA 2412 profile (m)

**D(y):** Flexural rigidity function, dependent on thickness (Nm)

**t:** Maximum thickness ratio from the NACA 2412 profile

**$k_s$ :** Shear correction factor

### Kinematics and Displacements

$w(x,y,t)$ : Transverse (out-of-plane) displacement of the mid-surface

$u(x,y,t), v(x,y,t)$ : In-plane (membrane) displacements in the  $x$  and  $y$  directions, respectively

$\theta_x(x,y,t), \theta_y(x,y,t)$ : Rotations of the transverse normal about the  $y$  and  $x$ -axes, respectively

$K_x, K_y, K_{xy}$ : Curvature and twist components of the plate

$\epsilon_x, \epsilon_y, \gamma_{xy}$ : In-plane normal and shear strain components

## Energy and Vibration

$U$ : Total potential (strain) energy of the system

$T$ : Total kinetic energy of the system

$\omega$ : Natural circular frequency (rad/s)

$f$ : Natural frequency (Hz)

$K$ : Global stiffness matrix

$M$ : Global mass matrix

$Q$ : Global vector of generalized coordinates

## Basis Functions and Eigenvalues

$X_i(x)$ : Spanwise basis function for the  $i$ -th mode, representing a clamped-free beam

$Y_j(y)$ : Chordwise basis function for the  $j$ -th mode, representing a free-free beam

$\lambda_i$ : Eigenvalues (roots) for the clamped-free beam characteristic equation

$\gamma_1, \gamma_2$ : Eigenvalues (roots) for the even and odd free-free beam characteristic equations, respectively

$\sigma_i$ : Shape parameter for the  $i$ -th clamped-free beam mode shape

## 1. Introduction

Modern turbomachinery is designed to be lighter and more efficient, but these same qualities make compressor blades more sensitive to vibration. Vibration remains a critical issue because it directly affects both the reliability and safety of the machine. Blades are exposed to aerodynamic forces, centrifugal loads, and thermal effects, any of which can trigger resonance. When vibration becomes excessive, it can cause high-cycle fatigue, initiate cracks, and in extreme cases, lead to catastrophic blade failure [1]. Such failures go beyond the loss of a single blade, they can threaten the integrity of the entire engine. Past studies, including the reported high-cycle fatigue failure of a high-pressure compressor blade due to resonant bending stresses [2], clearly show how vibratory loads can grow into serious damage. These risks highlight the importance of accurately predicting natural frequencies and mode shapes when designing compressor blades.

The accuracy of plate theories in vibration analysis depends on how well they capture shear effects. The Kirchhoff–Love model assumes that transverse normals remain perpendicular to the mid-surface, which works for very thin plates but becomes less reliable for moderately thick structures like compressor blades. In such cases, shear flexibility alters stiffness and frequency predictions, often leading to underestimation when neglected [3]. The Reissner–Mindlin or first-order shear deformation theory (FSDT) addresses this

by including transverse shear deformation and rotary inertia, offering a more realistic representation. Recent numerical studies on variable-thickness plates confirm that FSDT provides closer agreement with detailed simulations than the classical theory [4], making it a more suitable choice for blade-like geometries.

The Rayleigh–Ritz method has long been used as an efficient semi-analytical approach for plate and shell vibration problems [5]. By expanding displacement fields into admissible trial functions and applying energy principles, it reduces the problem to a generalized eigenvalue system. Its strength lies in capturing fundamental modes with relatively few terms, offering accuracy at lower computational cost compared to full finite element models. Early studies established its effectiveness for skew and variable-thickness plates [6,7], while more recent applications extend to anisotropic and viscoelastic structures. For compressor blades with complex geometry, Rayleigh–Ritz provides a practical balance of clarity and efficiency.

The reliability of Rayleigh–Ritz solutions depends strongly on the choice of admissible functions. For blade-like structures, functions based on beam and plate modes are advantageous since they inherently satisfy clamped and free-edge conditions, reducing the number of terms needed for convergence. Low-order modes are generally captured with few trial functions, whereas higher modes require richer expansions to represent localized effects. Convergence is especially sensitive to stiffness gradients and thickness variations, as reported in [8,9], making careful selection of admissible functions essential for realistic vibration modeling.

The thickness distribution of a blade strongly influences stiffness and natural frequencies. Simplified uniform models can capture overall trends but fail to reproduce local stiffness variations that affect mode predictions. Realistic airfoil shapes such as the NACA 2412, with its 12% maximum thickness and camber [11], provide a practical basis for modeling compressor blades. Studies have shown that even small deviations in thickness profiles can shift frequency predictions by several percent [10], underscoring the importance of using airfoil-based distributions for reliable vibration analysis.

Finite element analysis (FEA) is the industrial standard for blade vibration due to its ability to capture complex geometry and boundary conditions, but it comes at a high computational cost. In contrast, Rayleigh–Ritz offers a reduced-order framework that captures fundamental frequencies with good accuracy using far fewer degrees of freedom. Comparative studies report strong agreement between Ritz and FEM for the first few modes, with differences mainly appearing in higher-order localized modes [12,13]. This makes Rayleigh–Ritz especially useful for preliminary design and parametric studies where efficiency is critical.

Beyond frequency predictions, examining how modal energy is distributed among bending, shear, and membrane components provides valuable physical insight. This partitioning allows classification of modes into bending-dominated, shear-dominated, or in-plane membrane types, each carrying different structural risks. For instance, bending modes can cause large transverse displacements, while in-plane modes are linked to high stress concentrations. Recent studies show that energy partitioning reveals mode characteristics not always clear from frequency data alone [14,15], making it a powerful tool for compressor blade vibration analysis.

Boundary conditions strongly influence the dynamic response of compressor blades. In practice, the blade root is clamped into the disk while the other edges are free, which is realistically represented by the clamped–free–free–free (CFFF) condition. Studies show that even small changes in support, such as moving from cantilever to partially constrained edges, can significantly shift frequencies and alter mode order [16]. Free edges also promote in-plane and torsional modes at relatively low frequencies, making accurate boundary representation essential. Using admissible functions that inherently satisfy CFFF conditions within the Rayleigh–Ritz method improves accuracy while reducing the need for artificial constraints [17].

While Rayleigh–Ritz remains a cornerstone of semi-analytical modeling, recent trends combine it with data-driven or reduced-order methods to improve speed and accuracy. Machine learning has been used to predict blade frequencies once trained on simulation datasets [18], and hybrid Ritz–experimental approaches have shown promise in aeroelastic studies [19]. These methods offer significant efficiency gains over pure FEM while retaining essential physical insight, making them attractive for modern compressor design cycles that demand rapid iteration.

Although finite element analysis remains the dominant tool in industry, semi-analytical methods such as the Rayleigh–Ritz approach continue to offer distinct advantages. They are efficient, physically transparent, and well-suited for incorporating realistic boundary conditions and thickness variations without the heavy computational cost of full-scale models. In this work, we build on these strengths by developing a Rayleigh–Ritz framework based on Reissner–Mindlin plate theory to study the vibration of compressor blades modeled with a NACA 2412 thickness profile. Particular attention is given to classifying vibration modes through energy partitioning and displacement diagnostics, which not only improves frequency predictions but also provides a clearer physical picture of blade dynamics. This combination of efficiency, accuracy, and interpretability makes the approach a valuable complement to high-fidelity numerical simulations in the compressor blade design process.

## 2. Theoretical Formulations

The Reissner-Mindlin formulation governs the vibration response of the blade by balancing kinetic and strain energies within a variational framework. According to Hamilton's principle, the total action is expressed as the time integral of the difference between kinetic and potential energy. The equations of motion are obtained by taking the first variation of this functional, linking the transverse displacement, in-plane displacements, and rotational degrees of freedom. By incorporating bending, transverse shear, and in-plane membrane effects, the model is able to represent both flexural and in-plane vibration modes in a unified manner.

### 2.1 Governing Equations

The vibration behavior of the compressor blade is modeled using the Reissner-Mindlin plate theory, which accounts for both bending and transverse shear deformations. Unlike the classical Kirchhoff plate theory, which neglects transverse shear, the Reissner-Mindlin formulation accounts for shear effects, providing a more accurate representation for moderately thick blades. Consider a blade of span length  $a$  and chord length  $b$ , with a thickness distribution defined by the NACA 2412 airfoil profile. The governing equations for free vibration are derived from Hamilton's principle, which states that the variation of the action integral over time vanishes:

$$\delta \int_{t_0}^{t_1} (T - U) dt = 0$$

where  $T$  is the kinetic energy and  $U$  is the potential energy of the blade. The total potential energy  $U$  comprises bending ( $U_b$ ), transverse shear ( $U_s$ ), and in-plane membrane ( $U_m$ ) components:

$$U = U_b + U_s + U_m$$

### 2.2 Energy Expressions

For a compressor blade modeled as a moderately thick plate with variable thickness, the total strain energy arises from three primary sources: bending, transverse shear, and in-plane membrane deformations. These contributions are expressed in terms of the displacement field  $(u, v, w)$  and the rotational degrees of freedom  $(\theta_x, \theta_y)$  defined in the Reissner-Mindlin framework.

## 2.2.1 Bending Energy

The bending strain energy is associated with the curvature of the mid-surface and the corresponding bending stiffness coefficients. It is written as:

$$U_b = \frac{1}{2} \iint_{\Omega} (D_{11}\kappa_x^2 + D_{22}\kappa_y^2 + 2D_{12}\kappa_x\kappa_y + 2D_{66}\kappa_{xy}^2) dx dy$$

where  $\kappa_x = \frac{\partial\theta_x}{\partial x}$ ,  $\kappa_y = \frac{\partial\theta_y}{\partial y}$ , and  $\kappa_{xy} = \frac{\partial\theta_x}{\partial y} + \frac{\partial\theta_y}{\partial x}$  denote the curvatures and twist of the plate. The coefficients  $D_{ij}$  are elements of the bending stiffness matrix, defined as functions of the spatially varying thickness  $h(y)$ .

$$D_{11} = D_{22} = \frac{Eh(y)^3}{12(1-v^2)}, D_{12} = vD_{11}, D_{66} = \frac{Eh(y)^3}{12(1+v)}$$

## 2.2.2 Shear Energy

The transverse shear strain energy accounts for the relative rotation of the plate normal compared with the slope of the transverse displacement:

$$U_s = \frac{1}{2} \iint_{\Omega} k_s G h \left[ \left( \theta_x - \frac{\partial w}{\partial x} \right)^2 + \left( \theta_y - \frac{\partial w}{\partial y} \right)^2 \right] dx dy,$$

where  $k_s = \frac{5}{6}$  is the shear correction factor and  $G = \frac{E}{2(1+v)}$  is the shear modulus. This term becomes particularly important for thick or non-uniform sections, such as compressor blades with significant thickness variation.

## 2.2.3 Membrane Energy

The membrane energy results from in-plane deformations of the blade surface, and is expressed as:

$$U_m = \frac{1}{2} \iint_{\Omega} (N_x \epsilon_x + N_y \epsilon_y + 2N_{xy} \gamma_{xy}) dx dy$$

where  $\epsilon_x, \epsilon_y$  are normal in-plane strains,  $\gamma_{xy}$  is the in-plane shear strain, and  $N_x, N_y, N_{xy}$  are the corresponding membrane stress resultants.

## 2.2.4 Kinetic Energy

The total kinetic energy of the blade is given by:

$$T = \frac{1}{2} \iint_{\Omega} \left[ \rho h (\dot{w}^2 + \dot{u}^2 + \dot{v}^2) + \frac{\rho h^3}{12} (\dot{\theta}_x^2 + \dot{\theta}_y^2) \right] dx dy$$

where  $\rho$  is the mass density of the material,  $\dot{w} = \frac{\partial w}{\partial t}$  is the time derivative of the transverse displacement,  $\dot{u} = \frac{\partial u}{\partial t}$  and  $\dot{v} = \frac{\partial v}{\partial t}$  are time derivatives of in-plane displacements,  $\dot{\theta}_x, \dot{\theta}_y$  are time derivatives of rotational angles. The terms include translational inertia from both in-plane and out-of-plane displacements, as well as rotational inertia contributions.

## 2.2.5 Total Energy Functional

The complete energy functional of the system is therefore:

$$\Pi = U - T = U_b + U_s + U_m - T$$

which, when minimized using the Rayleigh-Ritz method, yields the discrete eigenvalue problem for the natural frequencies and associated mode shapes.

### 2.3 Modal Energy Distribution

To further characterize the computed modes beyond frequency values, an energy-based partition analysis were performed. The percentage contribution of bending ( $E_b$ ), shear ( $E_s$ ), and membrane ( $E_m$ ) were calculated according to:

$$E_b = \frac{U_b}{U} \times 100\%,$$

$$E_s = \frac{U_s}{U} \times 100\%,$$

$$E_m = \frac{U_m}{U} \times 100\%$$

where  $U_b, U_s, U_m$  are the bending, shear, and membrane strain energies, and  $U$  is the total modal energy. This partitioning identifies whether a mode is dominated by bending, shear, or in-plane membrane deformations.

### 2.4 Rayleigh–Ritz Approximation

The free vibration problem is solved using the Rayleigh-Ritz method, where the displacement fields are approximated by a finite series of separable basis functions. In the present study, the transverse displacement  $w(x,y,t)$  and the rotations  $\theta_x(x,y,t), \theta_y(x,y,t)$  are expanded as series of spatial basis functions multiplied by generalized coordinates:

$$w(x,y,t) \approx \sum_{i=1}^{N_{\text{bend}}} \sum_{j=1}^{N_{\text{bend}}} q_{ij}(t) X_i(x) Y_j(y),$$

$$\theta_x(x,y,t) \approx \sum_{i=1}^{N_{\text{tors}}} \sum_{j=1}^{N_{\text{tors}}} r_{ij}(t) X_i(x) Y_j(y),$$

$$\theta_y(x,y,t) \approx \sum_{i=1}^{N_{\text{tors}}} \sum_{j=1}^{N_{\text{tors}}} s_{ij}(t) X_i(x) Y_j(y),$$

$$u(x,y,t) \approx \sum_{i=1}^{N_{\text{mem}}} \sum_{j=1}^{N_{\text{mem}}} u_{ij}(t) X_i(x) Y_j(y),$$

$$v(x,y,t) \approx \sum_{i=1}^{N_{\text{mem}}} \sum_{j=1}^{N_{\text{mem}}} v_{ij}(t) X_i(x) Y_j(y),$$

where  $X_i(x)$  and  $Y_j(y)$  are spanwise and chordwise trial functions, respectively (described in Sec. 3.1). The unknown coefficients  $\{q_{ij}, r_{ij}, s_{ij}, u_{ij}, v_{ij}\}$  serve as generalized coordinates and are determined by minimizing the total potential energy.

Substituting these expansions into the Reissner-Mindlin energy expressions and integrating over the blade domain leads to a generalized eigenvalue problem:

$$K Q = \omega^2 M Q$$

where  $K$  is the assembled stiffness matrix,  $M$  is the consistent mass matrix,  $\omega$  are the natural circular frequencies, and  $Q$  is the vector of generalized coordinates.

To facilitate comparison of vibration results independent of geometric and material scaling, the natural frequencies are also expressed in non-dimensional form( $\Omega$ ).

$$\Omega = \omega a^2 \sqrt{\frac{\rho h_r}{D}}, D = \frac{Eh_r^3}{12(1-v^2)}$$

where  $h_r = h_{\max}$  is the maximum (reference) thickness of the blade corresponding to the NACA profile. This non-dimensional frequency parameter provides a useful means to compare the present results with existing studies of plate and blade vibrations.

Gaussian quadrature is employed for accurate numerical integration, ensuring that the energy integrals are evaluated with sufficient precision for the variable thickness blade. This approach provides a flexible framework to capture both bending-dominated and in-plane deformation modes, allowing systematic truncation to balance computational efficiency and accuracy.

## 2.5 Boundary conditions

The compressor blade is modeled as a rectangular plate with clamped at the root ( $x = 0$ ) and free along the remaining edges ( $x = a, y = 0, y = b$ ), denoted as CFFF boundary condition. The clamped root enforces zero displacements and rotations:

$$w(0,y) = 0, \quad \theta_x(0,y) = 0, \quad \theta_y(0,y) = 0, \quad u(0,y) = 0, \quad v(0,y) = 0$$

The free edges are naturally stress-free, as dictated by the variational formulation. The trial functions are designed to exactly satisfy the clamped conditions at the root, while allowing the free edges to deform without restriction.

## 2.6 Thickness Distribution from NACA 2412 Airfoil

The thickness distribution of the NACA 2412 airfoil is derived from its standardized geometric formulation[11].

For a normalized chordwise coordinate the one-sided thickness  $t_s(y)$  is given by:

$$t_s(y) = 5 \cdot t \cdot b \left( 0.2969\sqrt{y_n} - 0.1260y_n - 0.3516y_n^2 + 0.2843y_n^3 - 0.1015y_n^4 \right)$$

Where,  $y_n = \frac{y}{b}$  (where  $b$  is the chord length),  $t$  is the maximum thickness ratio (12% for NACA 2412). Then, the total thickness  $h(y)$  is the sum of both sides:

$$h(y) = 2 \cdot t_s(y)$$

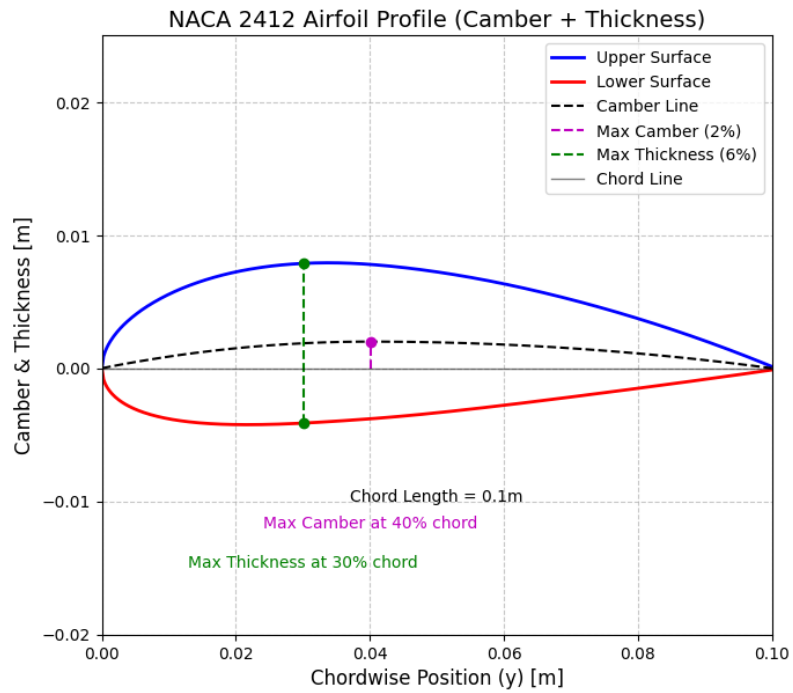


Fig.1. NACA 2412 airfoil profile

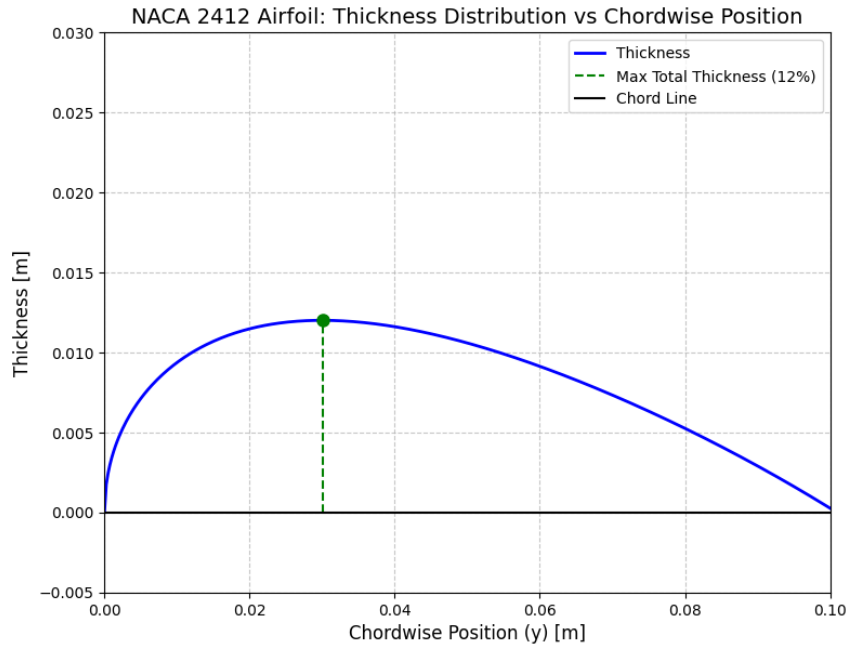


Fig.2. NACA 2412 airfoil thickness distribution vs chordwise position

### 3. Computational Implementation

The formulation was implemented numerically using the Rayleigh–Ritz method. The procedure begins with the expansion of displacement and rotation fields into admissible basis functions that satisfy the CFFF boundary condition. The stiffness and mass matrices are then assembled by evaluating the energy expressions through Gaussian quadrature. Solving the resulting generalized eigenvalue problem provides the natural frequencies and corresponding mode shapes of the blade. Following the eigenvalue analysis, post-processing is performed to extract additional information, including modal energy partitioning, which is used to classify the physical nature of each mode.

The entire framework was developed in Python, making use of standard scientific libraries: NumPy for array operations and numerical quadrature, SciPy for eigenvalue solvers, and Matplotlib for visualization. The resulting implementation is open-source, lightweight, and easily adaptable for extended studies of compressor blade vibration.

#### 3.1 Basis functions

The accuracy of the Rayleigh–Ritz method critically depends on the choice of trial functions. In the present study, separable functions are employed in spanwise and chordwise directions, ensuring conformity with the CFFF boundary condition (clamped at the root, free on all other edges).

##### 3.1.1 Spanwise direction (clamped–free):

The spanwise functions are constructed to satisfy the clamped–free conditions specified in Sec. 2.5. Spanwise functions are the classical clamped–free (cantilever) beam eigenfunctions scaled to span,  $x \in [0,a]$ . For the  $i$ -th spanwise mode we use the form [9]:

$$X_i(x) = \cosh\left(\frac{\lambda_i x}{a}\right) - \cos\left(\frac{\lambda_i x}{a}\right) - \sigma_i \left[ \sinh\left(\frac{\lambda_i x}{a}\right) - \sin\left(\frac{\lambda_i x}{a}\right) \right]$$

where,  $\lambda_i$  are the roots of the clamped–free characteristic equation

$$\cos \lambda_i \cdot \cosh \lambda_i + 1 = 0$$

Some of the roots are  $\lambda_1=1.875$ ,  $\lambda_2=4.694$ ,  $\lambda_3 = 7.854$ , etc. and the coefficient  $\sigma_i$  enforces the clamped end slope condition and is computed as

$$\sigma_i = \frac{\cosh \lambda_i + \cos \lambda_i}{\sinh \lambda_i + \sin \lambda_i}$$

These functions satisfy  $X_i(0) = X_i'(0) = 0$  (clamped at the root) and are free at  $x = a$  in the sense of the variational formulation.

##### 3.1.2 Chordwise (free–free) functions

Chordwise functions are selected to represent both symmetric and antisymmetric shapes on the free–free interval  $y \in [0,b]$ . It uses three types [9]:

1. Low-order special polynomials ( $j = 0$  and  $j = 1$ )

$$Y_0(y) = 1,$$

$$Y_1(y) = \left(1 - \frac{2y}{b}\right)$$

These two functions provide a constant and a linear-like anti-symmetric variation with convenient orthogonality and scaling for low-order modes.

2. Even-index free-free eigenfunction family ( $j = 2, 4, 6, 8, \dots$ ):

$$Y_j(y) = \cos\left(\gamma_1\left(\frac{y}{b} - \frac{1}{2}\right)\right) + \frac{\sin\frac{\gamma_1}{2}}{\sinh\frac{\gamma_1}{2}} \times \cosh\left(\gamma_1\left(\frac{y}{b} - \frac{1}{2}\right)\right)$$

where  $\gamma_1$  are roots of

$$\tan\left(\frac{\gamma_1}{2}\right) + \tanh\left(\frac{\gamma_1}{2}\right) = 0$$

3. Odd-index free-free eigenfunction family ( $j = 3, 5, 7, \dots$ ):

$$Y_j(y) = \sin\left(\gamma_2\left(\frac{y}{b} - \frac{1}{2}\right)\right) + \frac{\cos\frac{\gamma_2}{2}}{\cosh\frac{\gamma_2}{2}} \times \sinh\left(\gamma_2\left(\frac{y}{b} - \frac{1}{2}\right)\right)$$

where  $\gamma_2$  are roots of

$$\tan\left(\frac{\gamma_2}{2}\right) - \tanh\left(\frac{\gamma_2}{2}\right) = 0$$

The roots of the characteristic equations are determined using the Newton-Raphson method.

### 3.1.3 Composite Two-Dimensional Basis and Field Representation

Each displacement and rotation field is expressed as a series of admissible functions multiplied by generalized coordinates[20], following the Rayleigh–Ritz expansion in Sec. 2.4. The two-dimensional trial functions are constructed as separable products of the spanwise functions  $X_i(x)$  (Sec. 3.1.1) and the chordwise functions  $Y_j(y)$  (Sec. 3.1.2):

$$\Phi(x, y) = X_i(x) Y_j(y)$$

The same functional form is used for all fields, but with independent truncation orders for different types of motion:

$N_{bend}$  terms for the transverse displacement  $w(x, y)$ ,

$N_{tors}$  terms for the rotations  $\theta_x(x, y)$  and  $\theta_y(x, y)$  and

$N_{mem}$  terms for the in-plane displacements  $u(x, y)$  and  $v(x, y)$ .

This separation provides flexibility to refine the approximation according to the dominant deformation mode while ensuring that the basis functions automatically satisfy the clamped-free boundary conditions along the root and free edges.

## 3.2 Stiffness and Mass Matrix Formulation

Using the Rayleigh-Ritz approximations for the displacement fields, the total potential energy  $U$  and kinetic energy  $T$  of the blade can be written as:

$$U = U_{bend} + U_{shear} + U_{membrane},$$

$$T = T_{\text{transverse}} + T_{\text{rotational}} + T_{\text{in-plane}}$$

### 3.2.1 Stiffness Matrix

The total stiffness matrix  $K$  is assembled by summing contributions from bending, transverse shear, and in-plane (membrane) deformations:

$$K = K_{\text{bend}} + K_{\text{shear}} + K_{\text{mem}}$$

where the individual components are computed as

$$[K_{\text{bend}}]_{pq} = \iint_{\Omega} \left[ D \left( k_x^{(p)} k_x^{(q)} + k_y^{(p)} k_y^{(q)} + v \left( k_x^{(p)} k_y^{(q)} + k_y^{(p)} k_x^{(q)} \right) + \frac{1-v}{2} k_{xy}^{(p)} k_{xy}^{(q)} \right) \right] dx dy,$$

$$[K_{\text{shear}}]_{pq} = \iint_{\Omega} kGh [ \gamma_{xz}^p \gamma_{xz}^q + \gamma_{yz}^p \gamma_{yz}^q ] dx dy,$$

$$[K_{\text{mem}}]_{pq} = \iint_{\Omega} \epsilon^{(p)T} A \epsilon^{(q)} dx dy$$

Here:

$h = h(y)$  is the NACA 2412 airfoil thickness (defined in sec. 2.6),

$D = \frac{Eh^3}{12(1-v^2)}$  is the bending rigidity,

$kGh$  is the transverse shear rigidity ( $k$  is the shear correction factor),

$$\text{The membrane stiffness matrix, } A = \frac{Eh}{1-v^2} \begin{bmatrix} 1 & v & 0 \\ v & 1 & 0 \\ 0 & 0 & \frac{1-v}{2} \end{bmatrix},$$

The curvature component  $k_x, k_y, k_{xy}$  are obtained from the derivatives of the rotation fields  $\theta_x(x,y)$  and  $\theta_y(x,y)$  within the Reissner–Mindlin formulation.

The transverse shear strain components are defined as  $\gamma_{xz} = \frac{\partial w}{\partial x} - \theta_x$ , and  $\gamma_{yz} = \frac{\partial w}{\partial y} - \theta_y$ , which represent the difference between the slope of the transverse displacement and the rotation of the plate normal.

The in-plane strain vector,  $\epsilon = \left[ \frac{\partial u}{\partial x}, \frac{\partial v}{\partial y}, \frac{\partial u}{\partial y} + \frac{\partial v}{\partial x} \right]^T$

$p$  and  $q$  index the generalized coordinates corresponding to trial functions in the Rayleigh–Ritz expansion.

### 3.2.2 Mass Matrix

The consistent mass matrix  $M$  is assembled by integrating the kinetic energy over the plate domain:

$$M = M_{\text{transverse}} + M_{\text{rotational}} + M_{\text{in-plane}}$$

with components:

$$[M_{\text{transverse}}]_{pq} = \iint_{\Omega} \rho h \phi_p^w \phi_q^w dx dy,$$

$$[M_{\text{shear}}]_{pq} = \iint_{\Omega} \frac{\rho h^3}{12} (\phi_p^{\theta_x} \phi_q^{\theta_x} + \phi_p^{\theta_y} \phi_q^{\theta_y}) dx dy,$$

$$[M_{\text{mem}}]_{pq} = \iint_{\Omega} \rho h (\phi_p^u \phi_q^u + \phi_p^v \phi_q^v) dx dy.$$

where  $\rho$  is the material density, and  $\phi^w, \phi^{\theta_x}, \phi^{\theta_y}, \phi^u, \phi^v$  are the trial functions for transverse, rotational, and in-plane displacements.

Gaussian quadrature is used to evaluate all integrals numerically over the domain  $\Omega = [0, a] \times [0, b]$  with the NACA 2412 thickness  $h(y)$ .

#### 4. Modal Analysis using ANSYS

To validate the analytical results obtained from the Rayleigh-Ritz method, a numerical modal analysis was carried out using ANSYS Workbench. The main objective was to compute the natural frequencies and visualize the corresponding mode shapes of a compressor blade featuring a NACA 2412 airfoil profile. The numerical simulation was designed to closely follow the assumptions and parameters of the analytical model, ensuring consistency and enabling a direct comparison of results.

##### 4.1 Geometry

The compressor blade was modeled as a three-dimensional solid structure, with a constant spanwise length and a chordwise cross-section defined by the NACA 2412 airfoil. The airfoil coordinates were generated using the standard NACA 2412 equations, with a total of 100 points computed in Python. These points were imported into ANSYS and used to reconstruct the 3D geometry through extrusion along the span direction. The span and chord dimensions were carefully chosen to match the analytical model, allowing for a direct comparison of the predicted natural frequencies and mode shapes.

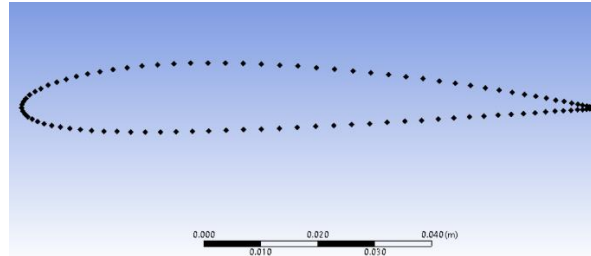


Fig.3. NACA 2412 airfoil profile points

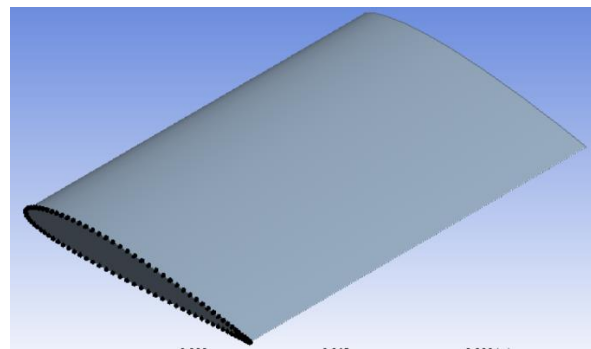


Fig.4. Compressor Blade Geometry

## 4.2 Meshing

The blade geometry was discretized using a structured mesh consisting of a combination of hexahedral and tetrahedral elements. The default meshing algorithm in ANSYS 2024 R1 was employed, resulting in a mesh with 7,297 nodes and 1,302 elements. This level of discretization was found to be adequate for accurately capturing the first few vibration modes.

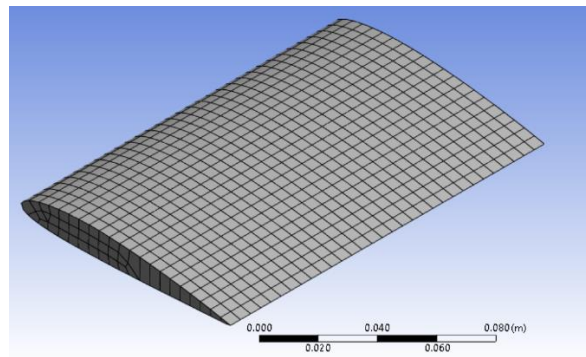


Fig.5. Compressor Blade Mesh

## 4.3 Simulation Setup and Boundary Conditions

Modal analysis was performed using the Modal module in ANSYS Mechanical. The blade material was modeled as isotropic and linearly elastic, with Young's modulus, Poisson's ratio, and density specified to match the values used in the Rayleigh-Ritz formulation.

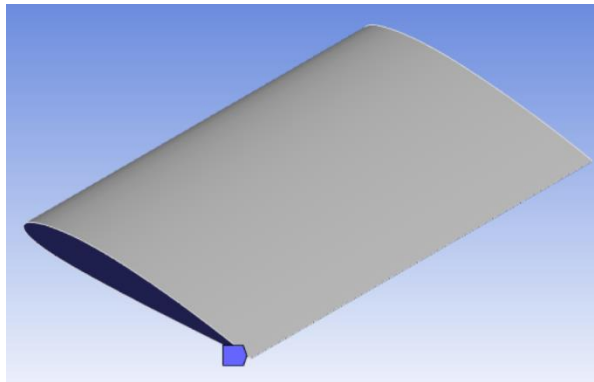


Fig.6. Boundary condition setup

The blade was constrained in a cantilever (clamped-free) configuration: the root face was fully fixed, with all translational and rotational degrees of freedom restrained, while the tip was left free to vibrate. This boundary condition replicates the classical clamped-free setup assumed in the analytical model.

## 4.4 Natural Frequencies and Mode Shapes

The modal analysis extracted the first ten natural frequencies and their associated mode shapes. The results were post-processed to visualize the deformation patterns in three dimensions, providing insight into both bending and torsional vibration characteristics of the blade.

## 5. Results and Discussion

### 5.1 Analysis Setup and Parameters

The analysis was conducted with the following geometric and material properties:

**Blade dimensions:** Length (a): 0.15 m, and Chord (b): 0.1 m

**Material properties:** Young's modulus (E): 200 GPa, Poisson's ratio (ν): 0.3, and Density (ρ): 7850 kg/m<sup>3</sup>

**Numerical resolution:** Gauss–Legendre quadrature with N = 16 integration points per axis was used for numerical evaluation of the stiffness and mass matrix entries.

**Basis functions and degrees of freedom:** The displacement and rotation fields were expanded using separable spanwise and chordwise basis functions. For simplicity, the same number of functions was used in all directions.

Transverse displacement w: n<sub>bend</sub> = 12 basis functions were used, resulting in N<sub>bend</sub> = n<sub>bend</sub><sup>2</sup> = 144 DOFs.

Rotations θ<sub>x</sub> and θ<sub>y</sub>: n<sub>tors</sub>=12 functions per field, giving N<sub>tors</sub>=144 DOFs each.

In-plane displacements u and v: n<sub>mem</sub>=12 functions per field, giving N<sub>mem</sub>=144 DOFs each.

The total number of generalized coordinates in the Rayleigh–Ritz system is therefore:

$$N_{\text{total}} = N_{\text{bend}} + 2N_{\text{tors}} + 2N_{\text{mem}} = 720$$

### 5.2 Comparison of Natural Frequencies

To evaluate the accuracy and effectiveness of the Rayleigh–Ritz method for modeling the free vibration of a compressor blade with NACA 2412 thickness distribution, the computed natural frequencies were compared against those obtained from finite element analysis (FEA) using ANSYS.

Table 1: Comparison of Natural Frequencies, ANSYS and Rayleigh–Ritz (n = 12)

Mode	Frequency (Hz)		% error
	ANSYS	RR	
1	373.31	377.45	1.11%
2	1373.80	1388.73	1.09%
3	2212.10	2248.29	1.64%
4	2498.40	2548.02	1.99%
5	4109.00	4191.55	2.01%
6	5450.40	5609.42	2.92%
7	6959.40	7393.75	6.24%
8	7506.20	7769.14	3.50%
9	8468.30	8556.30	1.04%
10	8600.10	9023.81	4.93%

The agreement is very good for the first six modes, where the error remains within below 3%. For higher modes, the discrepancy increases slightly, with errors of around 4–7% modes. This trend is expected since higher-order modes are more sensitive to local variations in stiffness and thickness, which are captured more accurately in the finite element model. Nevertheless, the overall comparison confirms that the Rayleigh–Ritz method, even with a moderate basis size (n = 12), provides reliable predictions of the blade's dynamic response.

### 5.3 Mode Shape Comparison

For visual comparison, the mode shapes from ANSYS and Rayleigh–Ritz method are presented. The  $n = 11$  results were chosen because, at  $n = 12$ , the mode shapes were inverted ( $180^\circ$  out of phase) relative to ANSYS. This inversion is purely a phase difference and does not change the modal deformation pattern. The following modes are scaled-up for better visualization.

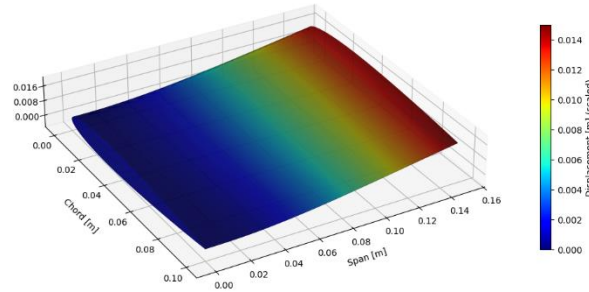


Fig.7. Mode 1 from Rayleigh-Ritz method

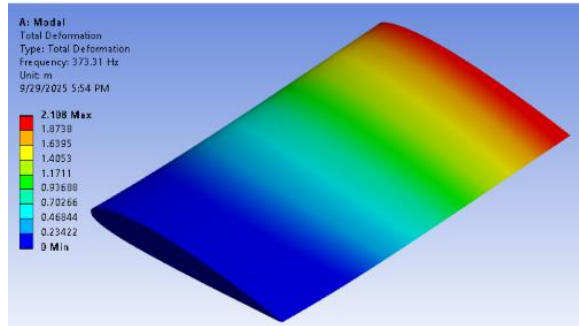


Fig.8. Mode 1 from ANSYS

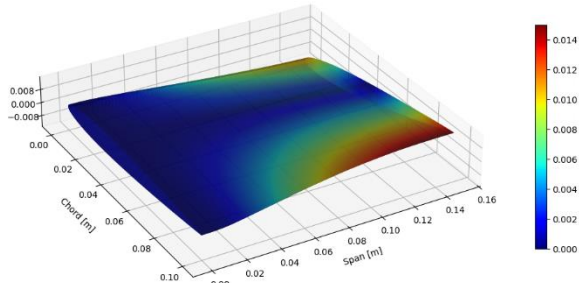


Fig.9. Mode 2 from Rayleigh-Ritz method

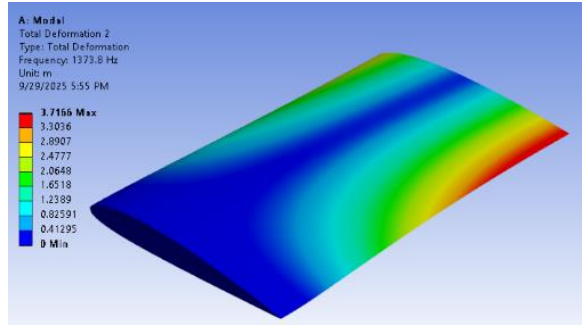


Fig.10. Mode 2 from ANSYS

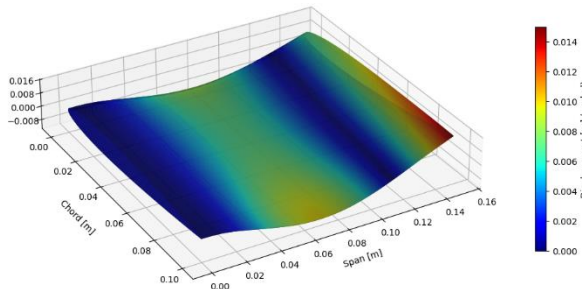


Fig.11. Mode 3 from Rayleigh-Ritz method

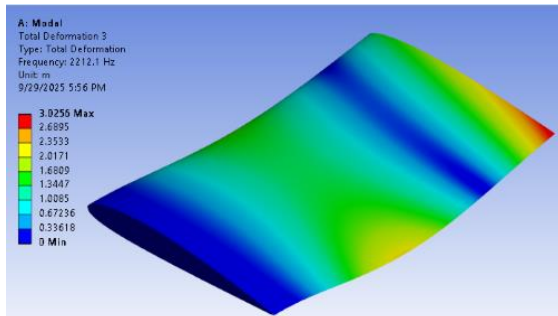


Fig.12. Mode 3 from ANSYS

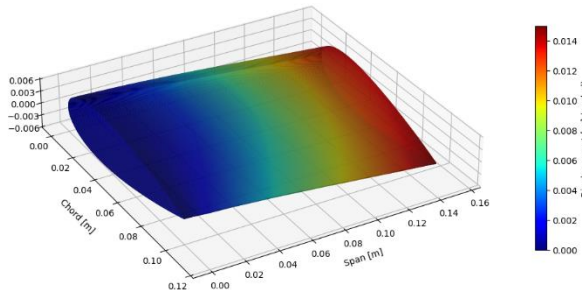


Fig.13. Mode 4 from Rayleigh-Ritz method

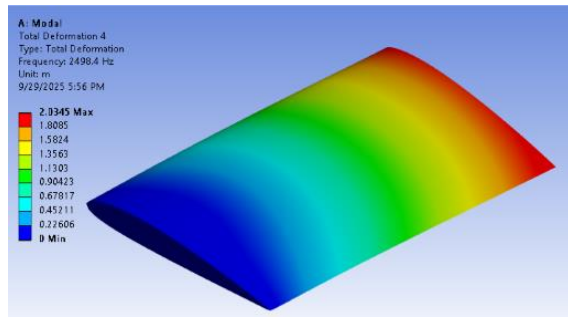


Fig.14. Mode 4 from ANSYS

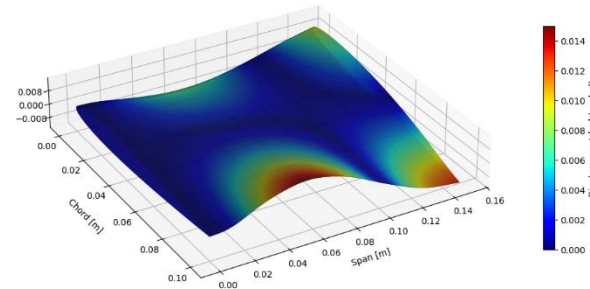


Fig.15. Mode 5 from Rayleigh-Ritz method

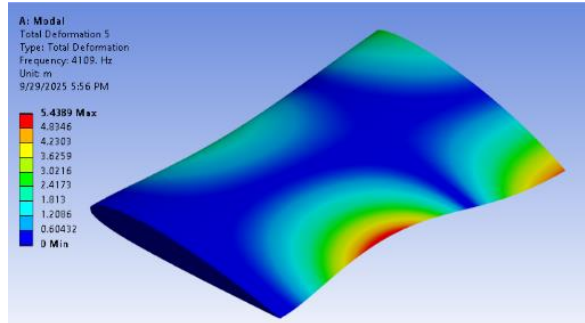


Fig.16. Mode 5 from ANSYS

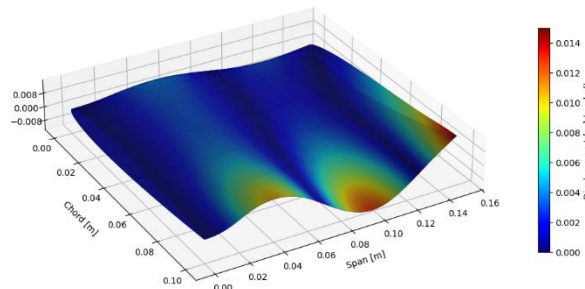


Fig.17. Mode 6 from Rayleigh-Ritz method

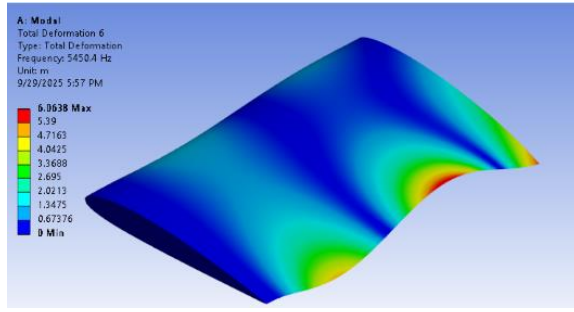


Fig.18. Mode 6 from ANSYS

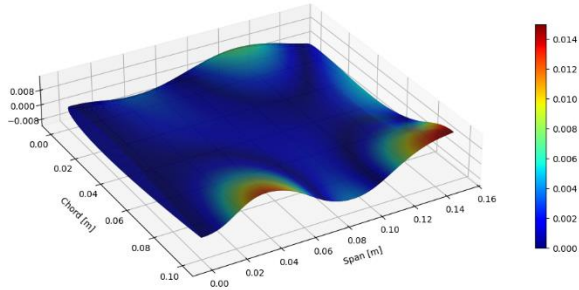


Fig.19. Mode 7 from Rayleigh-Ritz method

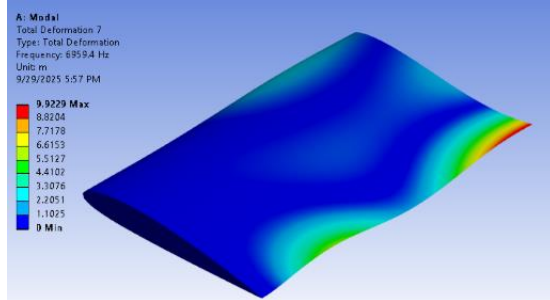


Fig.20. Mode 7 from ANSYS

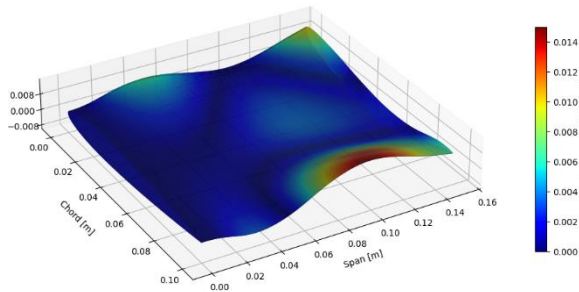


Fig.21. Mode 8 from Rayleigh-Ritz method

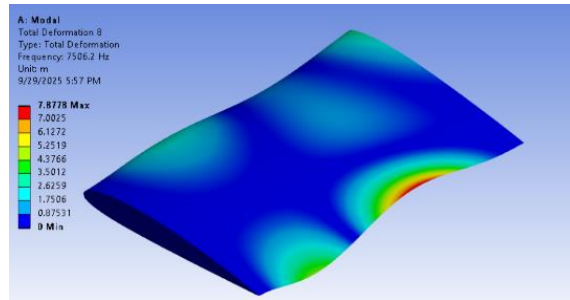


Fig.22. Mode 8 from ANSYS

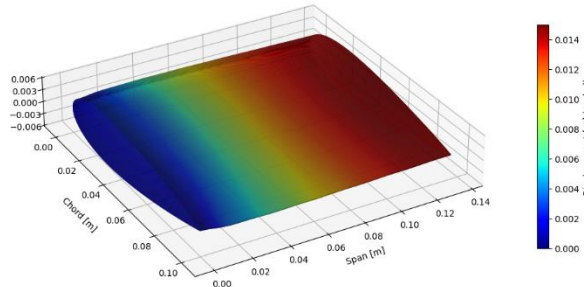


Fig.23. Mode 9 from Rayleigh-Ritz method

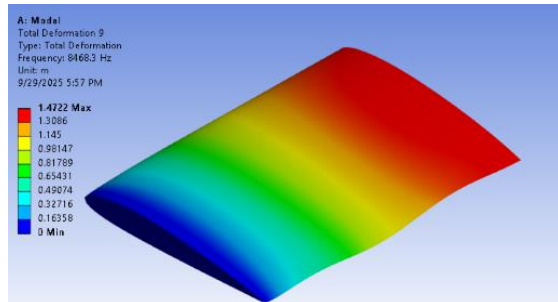


Fig.24. Mode 9 from ANSYS

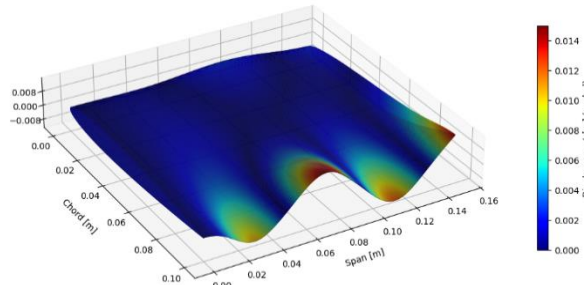


Fig.26. Mode 10 from Rayleigh-Ritz method

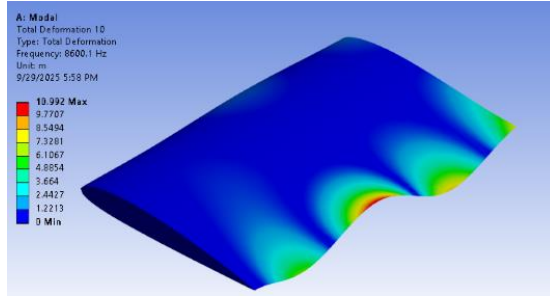


Fig.27. Mode 10 from ANSYS

Figures presented above are the first ten mode shapes of the compressor blade, arranged for direct comparison. For each mode, the ANSYS simulation result and the corresponding Rayleigh–Ritz result is shown. The comparison demonstrates excellent agreement between the two methods across bending-dominated, torsional, and in-plane modes. Key features, such as nodal lines and regions of maximum deflection, are well captured by the Rayleigh–Ritz method. Minor discrepancies are observed in the higher-order modes, where in-plane or membrane-dominated vibrations appear slightly exaggerated.

#### 5.4 Convergence Analysis

The graph illustrates how the Rayleigh–Ritz solution converges as the number of basis functions,  $n$ , increases. In general, the predicted frequencies settle toward stable values as additional terms are introduced.

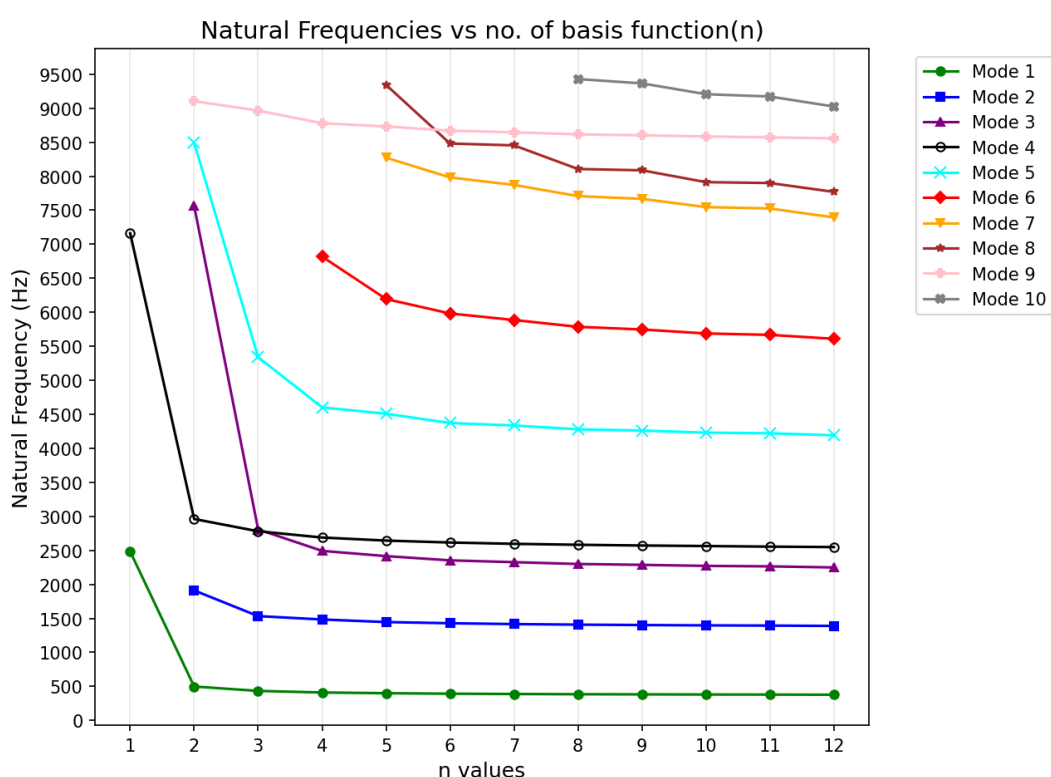


Fig.28. Natural frequencies vs n-values

The lowest modes converge the fastest: for instance, Mode 1 changes by less than 1% once ‘n’ exceeds 8, and by n = 12 the frequency has essentially stabilized at 377.45 Hz. Modes 2–5 follow the same pattern, with a steady, monotonic approach to their final values and differences of less than 2% between n = 10, n = 11, and n = 12. For higher modes (6–10), convergence is slower and the frequencies continue to shift by several percent even as the basis size grows. This is expected, since higher-order modes are more sensitive to both the richness of the chosen trial functions and to local stiffness variations arising from the NACA 2412 thickness distribution. Even so, the results show that using around 10–12 terms is sufficient to obtain reliable predictions for the lower modes, which are typically the most critical in compressor blade vibration studies.

Another important point is that some modes do not appear when the truncation order is small. For example, several higher modes are missing for n<5 and only appear once the basis is rich enough to represent their deformation patterns. This is a common feature of Rayleigh–Ritz approximations: the expansion must include sufficient terms before certain modes can be captured in the spectrum.

Accurate numerical integration is essential for higher truncation orders. When using n=13, the standard 16-point Gauss quadrature produced errors in higher-mode frequencies. To balance accuracy and computational efficiency, we performed most analyses with n=12, which provides converged results for the first ten modes.

Finally, it should be noted that only the ten lowest frequencies were extracted from the eigenvalue problem. As a result, at small values of n, some of the higher modes are not shown in the graph simply because the solver was restricted to reporting the lowest eigenvalues.

## 5.5 Modal Energy Distribution

The energy partitioning into bending, shear, and membrane contributions (introduced in Sec. 2.3) was computed for each mode.

Table 3. Modal energy distribution for first 10 modes for n = 12

<b>Mode</b>	<b>Eb%</b>	<b>Es%</b>	<b>Em%</b>
1	98.70%	1.30%	0.00%
2	95.20%	4.80%	0.00%
3	95.60%	4.40%	0.00%
4	0.00%	0.00%	100.00%
5	93.90%	6.10%	0.00%
6	92.30%	7.70%	0.00%
7	91.30%	8.70%	0.00%
8	90.50%	9.50%	0.00%
9	0.00%	0.00%	100.00%
10	90.30%	9.70%	0.00%

Table 3 summarizes the modal energy distribution for the first ten modes at n = 12. The results show that Modes 1–3 and 5–8 are dominated by bending, with more than 90% of their strain energy attributed to flexural deformation. These modes also exhibit moderate shear contributions (up to 9.5%), which become more pronounced in the higher bending modes. Modes 4 and 9, in contrast, are purely membrane-type modes, with 100% of their strain energy arising from in-plane deformations. Mode 10 continues the

bending-dominated pattern but shows the highest shear participation (9.7%), indicating stronger coupling between bending and shear effects at higher frequencies.

### 5.6 Effect of Aspect Ratio(a/b)

To examine the influence of geometry on the vibration characteristics, the aspect ratio ( $a/b$ ) of the simplified compressor blade was varied while keeping other parameters constant. The analysis was performed for the NACA 2412 thickness distribution using  $n = 6$  basis functions. Table 4 presents the non-dimensional frequency parameters ( $\Omega$ ) for the first eight modes across different aspect ratios.

Aspect Ratio $a/b$	Non dimensional Frequency ( $\Omega$ ) for Modes							
	1	2	3	4	5	6	7	8
4.0	3.07	19.21	23.45	28.20	54.56	85.54	104.47	126.09
3.0	3.06	18.89	21.41	22.91	52.77	65.03	99.06	112.77
2.0	3.04	14.37	18.67	21.61	43.48	50.57	76.59	89.07
1.5	3.03	11.02	18.15	20.17	33.72	46.14	61.56	65.41
1.0	3.01	7.68	16.79	17.34	24.03	29.97	36.92	44.59
0.5	2.87	4.31	8.87	11.40	11.81	14.66	16.87	20.38
0.2	1.86	2.68	3.00	3.77	5.22	5.39	6.37	6.58

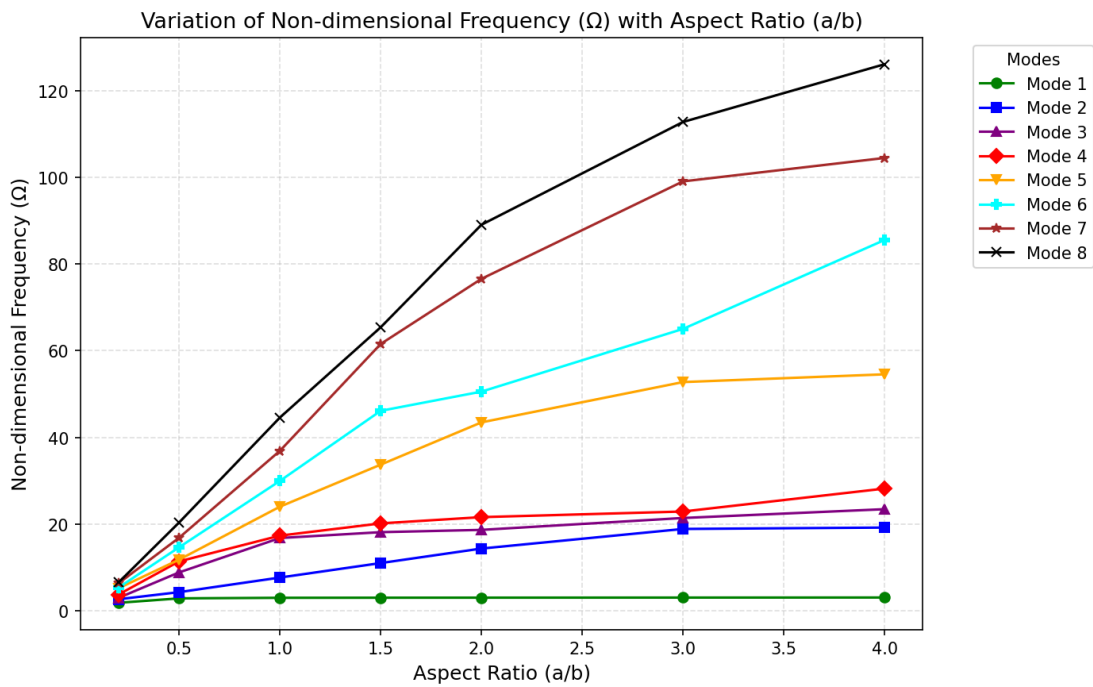


Fig.29. NACA 2412: Variation of non-dimensional frequency ( $\Omega$ ) with aspect ratio ( $a/b$ )

As the aspect ratio ( $a/b$ ) decreases, the plate becomes shorter in span compared to its chord, which causes the natural frequencies to drop noticeably. In other words, longer and thinner plates (with higher  $a/b$ ) are stiffer and vibrate at higher frequencies, while shorter and wider plates (with lower  $a/b$ ) are more flexible and vibrate more slowly. The first few vibration modes do not change much with aspect ratio, but the higher modes are more affected because of the increased influence of the plate's shape and shear effects.

## 6. Conclusion

This study presented a comprehensive free vibration analysis of a simplified compressor blade with a NACA 2412 thickness distribution using the Reissner–Mindlin plate theory combined with the Rayleigh–Ritz method. By employing admissible spanwise and chordwise basis functions that satisfy clamped–free–free boundary conditions, the approach provides an accurate yet computationally efficient representation of blade dynamics. The computed natural frequencies show excellent agreement with ANSYS finite element results, with the first six modes differing by less than 3% and higher-order modes within 5–7%. Convergence analysis confirmed that around eleven basis functions are sufficient to capture the essential dynamic behavior. Modal energy partitioning revealed bending-dominated modes, distinct in-plane membrane modes, and increasing shear participation at higher frequencies, offering valuable insight into potential resonance and structural risks.

Overall, the proposed semi-analytical framework can reliably model realistic compressor blade vibrations while significantly reducing computational effort compared to full finite element models. The method is well-suited for preliminary design, sensitivity studies, and optimization, and it can be extended in the future to include effects such as rotational stiffening, taper, twist, camber, thermal gradients, damping, and aerodynamic loading.

## References

- 1) Vibration characteristics of axial compressor blade under complex loading, Extrica (2022).
- 2) Failure Analysis of an Aeroengine High-Pressure Compressor Blade Due to High-Cycle Fatigue, Journal of Failure Analysis and Prevention (2018).
- 3) Reddy, J. N. (2007). Theory and Analysis of Elastic Plates and Shells. CRC Press.
- 4) Phung, V. H., Tran, M. T., & Nguyen, H. T. (2022). Numerical investigation on static bending and free vibration responses of two-layer variable thickness plates with shear connectors. Journal of Engineering Research, 9(3), 75–90.
- 5) Dawe, D. J., & Roufaeil, O. L. (1980). Rayleigh–Ritz vibration analysis of Mindlin plates. *Journal of Sound and Vibration*, \*69\*(3), 345–359.
- 6) Singh, B. N., & Saxena, V. (1997). Transverse vibration of skew plates with variable thickness. *Journal of Sound and Vibration*, 206(1), 1–18.
- 7) Sakiyama, T., & Huang, M. H. (1998). Free vibration analysis of plates with arbitrary variable thickness. *Journal of Sound and Vibration*, 216(2), 379–397.
- 8) Kumar, D., & Lal, R. (2024). Non-homogeneity effect on the vibration of the rectangular viscoelastic plate with quadratic thickness variation. *Acta Polytechnica*, 64(2), 241–252.
- 9) Leissa, A. W. (1969). Vibration of Plates. NASA SP-160, U.S. Government Printing Office.
- 10) Huang, M., & Sakiyama, T. (1996). Vibration of variable-thickness plates with realistic thickness profiles. *Journal of Sound and Vibration*, 192(5), 689–701.
- 11) Jacobs, E. N., Ward, K. E., & Pinkerton, R. M. (1933). The characteristics of 78 related airfoil sections from tests in the variable-density wind tunnel. NACA Report No. 460.
- 12) Rygiel, M., Obrocki, L., & Sieniawski, J. (2017). Numerical vibration analysis of turbine engine compressor blades using FEM. *Advances in Manufacturing Science and Technology*, 41(1), 5–15.
- 13) Liew, K. M., & Wang, C. M. (1993). Rayleigh–Ritz method for general plate analysis. *International Journal of Mechanical Sciences*, 35(12), 977–991.
- 14) Zhang, W. (2023). Transverse vibration of rectangular plates with arbitrary-shaped openings. *Journal of Physics: Conference Series*, 2455, 012011.
- 15) Seok, J., Tiersten, H. F., & Scarton, H. A. (2004). Free vibrations of rectangular cantilever plates. Part 2: In-plane motion. *Journal of Sound and Vibration*, 271(1–2), 147–158.

- 16) Warburton, G. B. (1954). The vibration of rectangular plates. Proceedings of the Institution of Mechanical Engineers, 168(1), 371–384.
- 17) Chaudhary, B. B., Chhantyal, B., & Luintel, M. C. (2024). Polynomial mode shape functions in free vibration analysis of cantilever Pelton turbines. Kathmandu Journal of Engineering and Management, 4(1), 92–101.
- 18) Wang, J., et al. (2022). Machine learning-based prediction of blade natural frequencies. Aerospace Science and Technology, 123, 107344.
- 19) Bakhtiari-Nejad, F., Rostami, H., & Dowell, E. H. (2020). Aeroelastic analyses of rectangular cantilever plates. Journal of Theoretical and Applied Vibration and Acoustics, 6(1), 103–118.
- 20) Reddy, J. N. (2007). *Theory and Analysis of Elastic Plates and Shells*, 2nd Edition, CRC Press.